



ATLAS Note

GROUP-2017-XX



24th September 2020

Draft version 0.1

1

2

Search for the Effects of Dimension-six

3

Operators in the interactions of the Higgs

4

Boson with the Top Quark

5

The ATLAS Collaboration

6 Several theories Beyond the Standard Model modify the momentum spectrum of the Higgs
7 Boson, without significantly altering the overall rate of Higgs produced from top quark pairs.
8 A differential measurement of the Higgs transverse momentum spectrum is performed for
9 events where the Higgs Boson is produced from top quark pairs and decays to final states
10 that include multiple leptons. The channels considered include two same-sign lepton and
11 three lepton final states. The momentum of the Higgs is predicted using a neural network,
12 based on the kinematics of its decay products. An effective field theory approach is used to
13 parameterize and place limits on the strength of potential six-dimensional operators.

© 2020 CERN for the benefit of the ATLAS Collaboration.

14 Reproduction of this article or parts of it is allowed as specified in the CC-BY-4.0 license.

Contents

16 Part I**17 Introduction****18 1 Introduction**

19 Particle physics is an attempt to describe the fundamental building blocks of the universe and
20 their interactions. The Standard Model (SM) - our best current theory of fundamental particle
21 physics - does a remarkable job of that. All known fundamental particles and (almost) all of the
22 forces underlying their interactions can be explained by the SM, and the predictions from this
23 theory agree with experiment to an incredibly precise degree. This is especially true since the
24 Higgs Boson, the last piece of the SM predicted decades before, was finally discovered at the
25 Large Hadron Collider (LHC) in 2012.

26 Despite the success of the SM, there remains significant work to be done. For one, the
27 SM is incomplete: it fails to provide a description of gravity, to give an explanation for the
28 observation of Dark Matter, or to provide a mechanism for neutrinos to gain mass. Further, a
29 Higgs Boson with a mass of around 125 GeV, as observed at the LHC, gives rise to what is
30 known a hierarchy problem - such a low mass Higgs requires a seemingly unnatural level of “fine
31 tuning” that is unexplained by the SM.

32 A promising avenue for addressing these problems is to study the properties of the Higgs
33 Boson and the way it interacts with other particles, in part simply because these interactions

34 have not been measured before. Its interactions with the Top Quark are a particularly promising
35 place to look. Because the Higgs Field is responsible for allowing particle to acquire mass, the
36 strength of a particle's interaction with the Higgs Boson is proportional to its mass. As the most
37 massive of the fundamental particles, the Top Quark has the strongest coupling to the Higgs
38 Boson, meaning any new physics in the Higgs sector is likely to present itself most prominently
39 in its interaction with the Top Quark.

40 These interactions can be measured by directly by studying the production of a Higgs
41 Boson in association with a pair of Top Quarks ($t\bar{t}H$). While studies have been done measuring
42 the overall rate of $t\bar{t}H$ production, there are several theories of physics Beyond the Standard
43 Model (BSM) that would affect the kinematics of $t\bar{t}H$ production without altering its overall
44 rate. This dissertation attempts to make a differential measurement of the kinematics of the
45 Higgs Boson in $t\bar{t}H$ events in order to search for these BSM effects.

46 An Effective Field Theory model can be used to model the low energy effects of high
47 energy physics.

48 The proton-proton collision data collected by the ATLAS detector at the LHC from 2015-
49 2018 provides the opportunity to make this measurement for the first time. The unprecedented
50 energy achieved by the LHC during this period greatly increase the rate at which $t\bar{t}H$ events are
51 produced, and the large amount of data collected provides the necessary statistics for a differential
52 measurement to be performed.

53 A study of $t\bar{t}H$ events with multiple leptons in the final state is performed, using 139 fb^{-1}

54 of data from proton-proton collisions at an energy $\sqrt{s} = 13$ TeV collected by the ATLAS detector
55 from 2015-2018. Events are separated into channels based on the number of light leptons in the
56 final state - either two same-sign leptons, or three leptons. A deep neural network is used to
57 reconstruct the momentum of the Higgs Boson in each event. This momentum spectrum is fit to
58 data for each analysis channel, the result of which is used to place limits on BSM effects.

59 This dissertation begins with a brief explanation of the SM, its limitations, and the theor-
60 etical motivation behind this work. This is followed by a description of the LHC and the ATLAS
61 detector. The analysis strategy is then described, and the results are presented. Finally, the results
62 of the study are summarized in the conclusion.

63 **Part II**

64 **Theoretical Motivation**

65 **2 The Standard Model and the Higgs Boson**

66 The Standard Model of particle physics (SM) is a Quantum Field Theory (QFT) describing the
67 known fundamental particles and their interactions. It accounts for three of the four known
68 fundamental force - electromagnetism, the weak nuclear force, and the strong nuclear force, but
69 not gravity. Further, the SM describes a mechanism for combining the weak and electromagnetic
70 forces into a singular interaction, known as the electroweak force. It is a non-Abelian gauge

⁷¹ theory, invariant under the Lie Group $SU(3)_C \otimes SU(2)_L \otimes U(1)_Y$, where C refers to color
⁷² charge, L, the helicity of the particle, and Y, the hypercharge.

⁷³ 2.1 The Forces and Particles of the Standard Model

⁷⁴ The SM particles, summarized in figure ??, can be classified into two general categories based
⁷⁵ on their spin: fermions, and bosons.

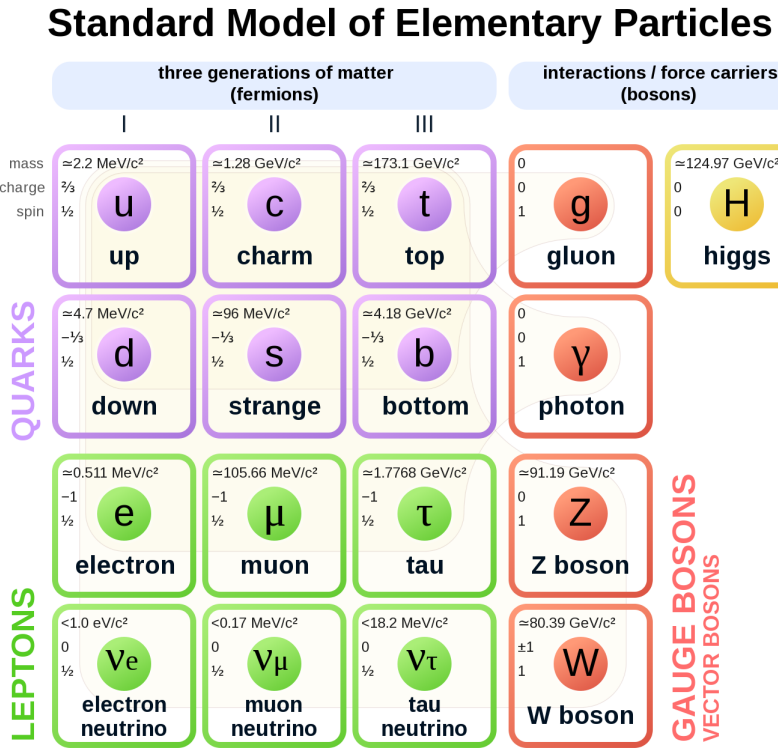


Figure 2.1: A summary of the particles of the Standard Model, including their mass, charge and spin, with the fermions listed on the left, and the bosons on the right. []

⁷⁶ Fermions are particles with $\frac{1}{2}$ -integer spin, which according to the spin-statistics theorem,
⁷⁷ causes them to comply with the Pauli-exclusion principle []. They can be separated into two

⁷⁸ groups, leptons and quarks, each of which consist of three generations of particles with increasing
⁷⁹ mass.

⁸⁰ Leptons are fermions interact via the electroweak force, but not the strong force. The three
⁸¹ generation of leptons consist of the electron and electron neutrino, the muon and muon neutrino,
⁸² the tau and tau neutrino. The quarks, which do interact via the strong force - which is to say they
⁸³ have color charge - in addition to the electroweak force. The three generations include the up
⁸⁴ and down quarks, the strange and charm quarks, and the top and bottom quarks. Each of these
⁸⁵ generations form left-handed doublets invariant under SU(2) transformations. For the leptons
⁸⁶ these doublets are:

$$\begin{pmatrix} e^- \\ \nu_e \end{pmatrix}_L, \begin{pmatrix} \mu^- \\ \nu_\mu \end{pmatrix}_L, \begin{pmatrix} \tau^- \\ \nu_\tau \end{pmatrix}_L \quad (2.1)$$

⁸⁷ And for the quarks:

$$\begin{pmatrix} u \\ d \end{pmatrix}_L, \begin{pmatrix} s \\ c \end{pmatrix}_L, \begin{pmatrix} t \\ b \end{pmatrix}_L \quad (2.2)$$

⁸⁸ For both leptons and quarks, the heavier generations can decay into the lighter generation
⁸⁹ of particles, while the first generation does not decay. Hence, ordinary matter generally consists
⁹⁰ of this first generation of fermions - electrons, up quarks, and down quarks. Each of these
⁹¹ fermions has a corresponding anti-particle, which has an equal mass as its partner but opposite

92 charge. The fermions acquire their mass via the Higgs Mechanism, except for the neutrinos,
93 whose mass has been experimentally confirmed but is not accounted for in the SM.

94 Bosons, by contrast, have integer spin, and are therefore unconstrained by the Pauli-
95 exclusion principle. The SM includes two kinds of bosons: Gauge bosons, which are spin-1
96 particles that mediate the interactions between the fermions, and a single scalar, i.e. spin-0,
97 particle - the Higgs Boson. Of the gauge bosons, the W^+ , W^- and Z bosons - which are the
98 mass eigenstates of the electroweak bosons - mediate the weak interaction, while the photon
99 mediates the electric force, and the gluon mediates the strong force.

100 **2.2 The Higgs Mechanism**

101 A key feature of the SM is the gauge invariance of its Lagrangian. However, any terms added to
102 the Lagrangian giving mass to the the gauge bosons would violate the underlying symmetry of
103 the theory. This presents a clear problem with the theory: The experimental observation that the
104 W and Z bosons have mass seems to contradict the basic structure of the SM.

105 Rather than abandoning gauge invariance, an alternative way for particles to acquire mass
106 beyond adding a simple mass term to the Lagrangian was theorized by Higgs, Englert and Brout
107 in 1964 []. This procedure for introducing masses for the gauge bosons while preserving local
108 gauge invariance, known as the Higgs mechanism, was incorporated into the electroweak theory
109 by Weinberg in 1967 [].

¹¹⁰ **2.2.1 The Higgs Field**

¹¹¹ The Higgs mechanism introduces a complex scalar $SU(2)$ doublet, Φ , with the form:

$$\Phi = \begin{pmatrix} \phi^+ \\ \phi^0 \end{pmatrix}_L \quad (2.3)$$

¹¹² This field introduces a scalar potential to the Lagrangian of the form:

$$V(\Phi) = \mu^2 |\Phi^\dagger \Phi| + \lambda (|\Phi^\dagger \Phi|)^2 \quad (2.4)$$

¹¹³ Where μ and λ are free parameters of the new field. This represents the most general
¹¹⁴ potential allowed while preserving $SU(2)_L$ invariance and renormalizability. In the case that
¹¹⁵ $\mu^2 < 0$, this potential takes the form shown in figure ??.

¹¹⁶ The significant feature of this potential is that its minimum does not occur for a value of
¹¹⁷ $\Phi = 0$. Instead, it is minimized when $|\Phi^\dagger \Phi| = -\mu^2/\lambda$. This means that in its ground state, the
¹¹⁸ Higgs field takes on a non-zero value - referred to as a vacuum expectation value (VEV). So while
¹¹⁹ the Higgs potential is globally symmetric, about the minimum this symmetry is broken. Since

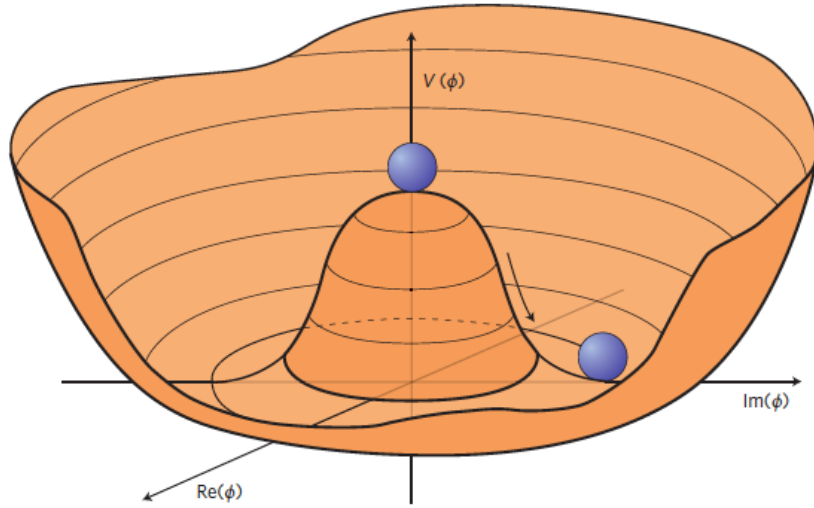


Figure 2.2: The value of the Higgs potential, $V(\Phi)$ as a function of Φ , for the case that $\mu^2 < 0$ [].

₁₂₀ the minimum is determined only by $\Phi^\dagger \Phi$, there is some ambiguity in the particular definition of
₁₂₁ the VEV, but it is generally represented as

$$\langle \Phi \rangle = \frac{1}{\sqrt{2}} \begin{pmatrix} 0 \\ v \end{pmatrix} \quad (2.5)$$

₁₂₂ The full value of Φ can be written as

$$\langle \Phi \rangle = \frac{1}{\sqrt{2}} \begin{pmatrix} 0 \\ v + H/\sqrt{2} \end{pmatrix} \quad (2.6)$$

₁₂₃ with v being the value of the VEV, and H being the real value of the scalar field.

¹²⁴ **2.2.2 Electroweak Symmetry Breaking**

¹²⁵ The Electroweak (EWK) interaction is described in the SM by a $SU(2)_L \otimes U(1)_Y$ gauge theory.
¹²⁶ This theory predicts three $SU(2)_L$ gauge boson, $W_\mu^1, W_\mu^2, W_\mu^3$, and a single $U(1)_Y$ gauge boson,
¹²⁷ B_μ . The couplings of these bosons to the Higgs field show up in the kinetic terms of the scalar
¹²⁸ field Φ in the Lagrangian:

$$(D_\mu \Phi)^\dagger (D^\mu \Phi) = |(\partial_\mu - \frac{ig}{2} W_\mu^a \sigma^a - \frac{ig'}{2} B_\mu Y) \phi|^2 \quad (2.7)$$

¹²⁹ Here D_μ represents the covariant derivative required to preserve gauge invariance, g and
¹³⁰ g' represent coupling constant of the gauge bosons, σ^a denotes the Pauli matrices of $SU(2)$,
¹³¹ and Y represents the hypercharge of $U(1)$. The terms in this interaction which contribute to the
¹³² masses of the gauge bosons can be written as:

$$\frac{1}{2}(0, v)(\frac{g}{2} W_\mu^a \sigma^a - \frac{g'}{2} B_\mu)^2 \begin{pmatrix} 0 \\ v \end{pmatrix} \quad (2.8)$$

¹³³ Expanding these terms into the mass eigenstates of the electroweak interaction yields four
¹³⁴ physical gauge bosons, two charged and two neutral, which are linear combinations of the fields

¹³⁵ $W_\mu^1, W_\mu^2, W_\mu^3$, and B_μ :

$$\begin{aligned} W_\mu^\pm &= \frac{1}{\sqrt{2}}(W_\mu^1 \pm iW_\mu^2) \\ Z^\mu &= \frac{1}{\sqrt{(g^2 + g'^2)}}(-g'B_\mu + gW_\mu^3) \\ A^\mu &= \frac{1}{\sqrt{(g^2 + g'^2)}}(gB_\mu + g'W_\mu^3) \end{aligned} \tag{2.9}$$

¹³⁶ And the masses of these fields are given by:

$$\begin{aligned} M_W^2 &= \frac{1}{4}g^2v^2 \\ M_Z^2 &= \frac{1}{4}(g^2 + g'^2)v^2 \\ M_A^2 &= 0 \end{aligned} \tag{2.10}$$

¹³⁷ This produces exactly the particles we observe - three massive gauge bosons and a single
¹³⁸ massless photon. The massless photon represents the portion of the gauge symmetry, a single
¹³⁹ $U(1)$ of the electromagnetic force, that remains unbroken by the VEV.

¹⁴⁰ Interactions with the Higgs field also lead to the generation of the fermion masses, which
¹⁴¹ in the Lagrangian take the form:

$$-\lambda_\psi(\bar{\psi}_L\phi\psi_R + \bar{\psi}_R\phi^\dagger\psi_L) \tag{2.11}$$

¹⁴² After symmetry breaking has occurred and ϕ has taken on the value of the VEV as written
¹⁴³ in equation ??, the mass terms of the fermions become $\lambda_\psi v$. Written this way, the fermion masses
¹⁴⁴ are proportional to their Yukawa coupling to the VEV, λ_ψ .

¹⁴⁵ Based on the equation ??, an additional mass term, $\mu^2 H^2$ arises from the potential $V(\Phi)$.
¹⁴⁶ This term can be understood as an excitation of the Higgs field, a scalar boson with mass $M_H = \mu$.
¹⁴⁷ This is the Higgs boson, which comes about as a natural prediction of electroweak symmetry
¹⁴⁸ breaking.

¹⁴⁹ The fermion's Yukawa coupling to the VEV take the same form as the fermion's coupling
¹⁵⁰ to the Higgs boson - λ_ψ . Therefore, the strength of a fermion's interaction with the Higgs is
¹⁵¹ directly proportional to its mass. We now have a model that predicts a Higgs boson with mass
¹⁵² $M_H = \mu$, which interacts with the fermions with coupling strength λ_ψ . Because μ and λ_ψ are
¹⁵³ free parameters of the theory, the mass of the Higgs boson and its interactions with the fermions
¹⁵⁴ must be measured experimentally.

¹⁵⁵ 2.3 Limitations of the Standard Model

¹⁵⁶ While the SM has great predictive power, there are still several experimental observations that the
¹⁵⁷ SM fails to explain. For example, the SM predicts neutrinos to be massless, despite experimental
¹⁵⁸ observation to the contrary.

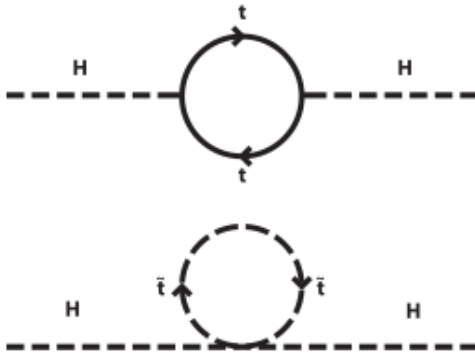


Figure 2.3: Above diagram is the leading order correction to the Higgs mass via a top quark loop, and below is the stop squark loop, coming from a supersymmetric extension of the SM, that provides a potential cancellation of the top diagram [6].

¹⁵⁹ **3 Effective Field Theory in $t\bar{t}H$ Production**

¹⁶⁰ Higher dimension operators are a common way to paramaterize the effects of physics at very
¹⁶¹ high energies into

¹⁶² **3.1 Extensions to the Higgs Sector**

¹⁶³ **3.2 Six Dimensional Operators**

¹⁶⁴ While the SM has been tested to great precision, particularly at the LHC, it is generally accepted
¹⁶⁵ that it is only valid up to a certain energy scale. It is assumed that above a certain energy, at the
¹⁶⁶ scale where something like a Grand Unified Theory (GUT) or quantum gravity become relevant,
¹⁶⁷ the SM will not be applicable.

Part III**169 The LHC and the ATLAS Detector****170 4 The LHC**

171 The Large Hadron Collider (LHC) is a particle accelerator consisting of a 27 km ring, designed
172 to collide protons at high energy. Located outside of Geneva, Switzerland and buried about 100
173 m underground, it consists of a ring of superconducting magnets which are used to accelerate
174 opposing beams of protons - or lead ions - which collide at the center of one of the various
175 detectors located around the LHC ring which record the result of these collisions. These
176 detectors include two general purpose detectors, ATLAS and CMS, which are designed to make
177 precision measurements of a broad range of physics phenomenon, and two more specialized
178 experiments, LHCb and ALICE, which are optimized to study b-quarks and heavy-ion physics,
179 respectively.

180 The LHC first began running in 2009 at a proton-proton center of mass energy of $\sqrt{s} = 8$
181 TeV. It operated at this energy from 2009 to 2012, known as Run 1, and data collected during
182 this period was used in discovering the Higgs Boson. The LHC began running again in 2015,
183 and collected data at an increased energy of $\sqrt{s} = 13$ TeV until 2018, a period referred to as Run
184 2.

185 The LHC consists of a chain of accelerators, which accelerate the protons to higher and

186 higher energies until they are injected into the main ring. This process is summarized in figure
 187 **??**. Protons extracted from a tank of ionized hydrogen are fed into a linear accelerator, LINAC2,
 188 where they reach an energy of 50 MeV. From there, they enter a series of three separate circular
 189 accelerators, before being injected into the main accelerator ring at an energy of 450 GeV. Within
 190 the main ring protons are separated into two separate beams moving in opposite directions,
 191 and their energy is increased to their full collision energy. Radiofrequency cavities are used to
 192 accelerate these particles and sort them into bunches. From 2015-2018, these bunches consisted
 193 of around 100 billion protons each with an energy of 6.5 TeV per proton, which collided at a rate
 194 of 40 MHz, or every 25 ns.

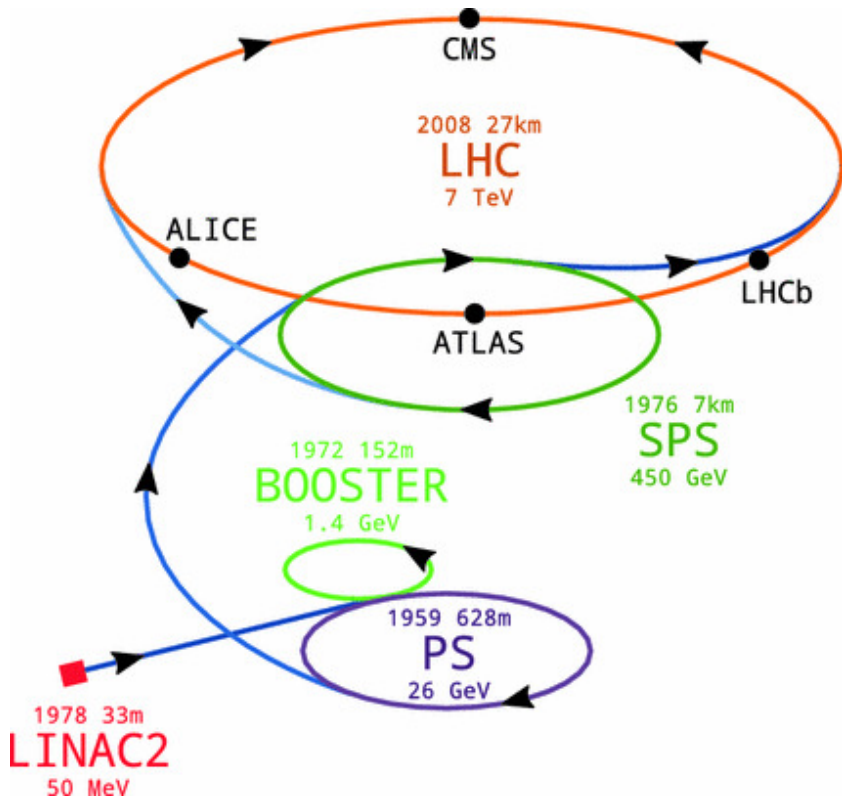


Figure 4.1: A summary of the accelerator chain used to feed protons into the LHC [].

195 Because these proton bunches consist of a large number of particles, each bunch crossing
 196 consists of not just one, but several direct proton-proton collisions. The number of interactions
 197 that occur per bunch crossing, μ , is known as pileup. During Run 2, the average pileup for bunch
 198 crossings was around $\langle \mu \rangle = 35$, with values typically ranging between 10 and 70.

199 The amount of data collected by the LHC is measured in terms of luminosity, which is the
 200 ratio of the number of events detected per unit time, $\frac{dN}{dt}$, and the interaction cross-section, σ .

$$\mathcal{L} = \frac{1}{\sigma} \frac{dN}{dt} \quad (4.1)$$

201 The design luminosity of the LHC is $10^{34} \text{ cm}^{-2} \text{ s}^{-1}$, however the LHC has achieved a
 202 luminosity of over $2 \times 10^{34} \text{ cm}^{-2} \text{ s}^{-1}$. The total luminosity is then this instantaneous luminosity
 203 integrated over time.

$$\mathcal{L}_{\text{int}} = \int \mathcal{L} dt \quad (4.2)$$

204 The integrated luminosity collected by the ATLAS detector as of the end of 2018 is around
 205 140 fb^{-1} , exceeding the expected integrated luminosity of 100 fb^{-1} .

206 5 The ATLAS Detector

207 ATLAS (a not terribly natural acronym for “A Toroidal LHC Apparatus”) is a general purpose
208 detector designed to maximize the detection efficiency of all physics objects, including leptons,
209 jets, and photons. This means it is capable of measuring all SM particles, with the exception of
210 neutrinos, the presence of which can be inferred based on missing transverse momentum. The
211 detector measures 44 m long, and 25 m tall.

212 The ATLAS detector consists of multiple layers, each of which serves a different purpose
213 in reconstructing collisions. At the very center of the detector is the interaction point where the
214 proton beams of the LHC collide.

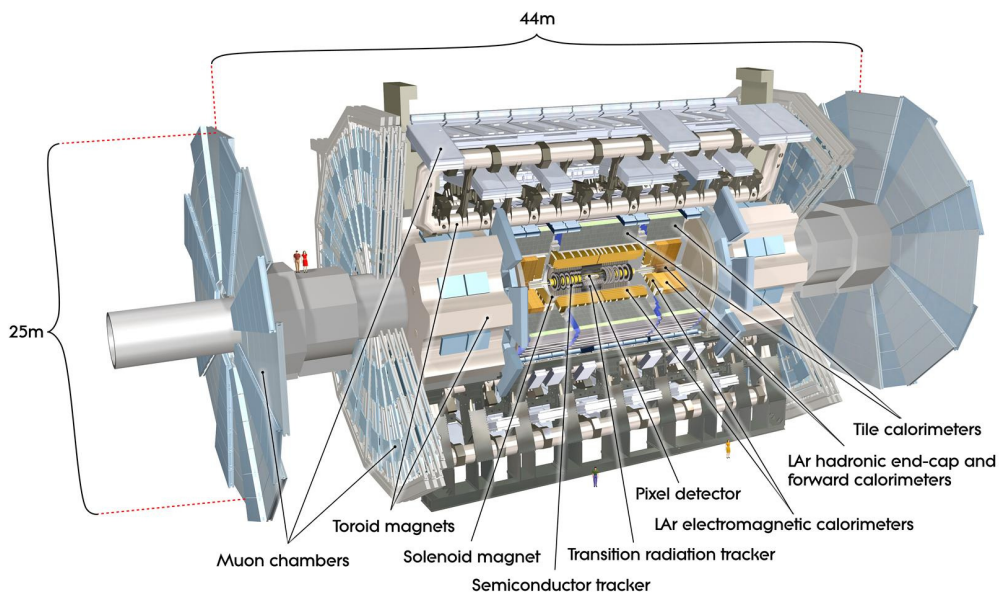


Figure 5.1: Cutaway view of the ATLAS detector, with labels of its major components [].

215 **5.1 Inner Detector**

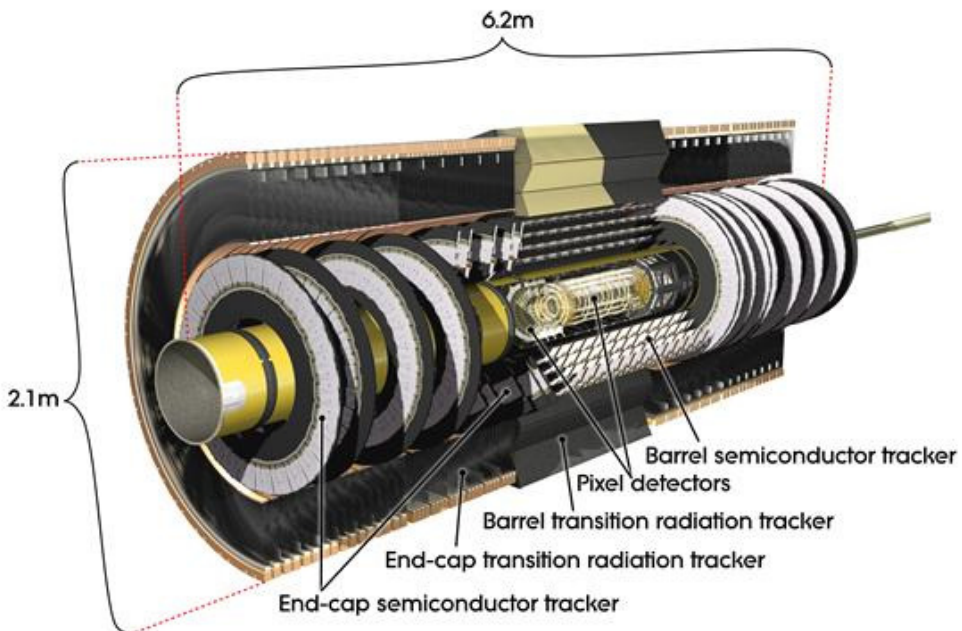


Figure 5.2: Cutaway view of the Inner Detector [].

216 Just surrounding the interaction point is the Inner Detector, designed to track the path
217 of charged particles moving through the detector. An inner solenoid surrounding the Innder
218 Detector is used to produces a magnetic field of 2 T. This large magnetic field causes the path
219 of charged particles moving through the Inner Detector to bend. Because this magnetic field is
220 uniform and well known, it can be used in conjunction with the curvature of a particles path to
221 measure its charge and momentum.

222 The Inner Detector consists of three components - the Pixel Detector, the Semi-Conductor
223 Tracker (SCT), and the Transition Radiation Tracker (TRT). The Pixel Detector is the innermost
224 of these, beginning just 33.25 mm away from the beam line. It consists of three silicon layers

225 along the barrel, as well as three endcap layers, covering a range of $|\eta| < 2.5$.

226 The Semiconductor Tracker (SCT) is similar to the Pixel detector, but uses long strips
 227 rather than small pixel to cover a larger spatial area.

228 **5.2 Calorimeters**

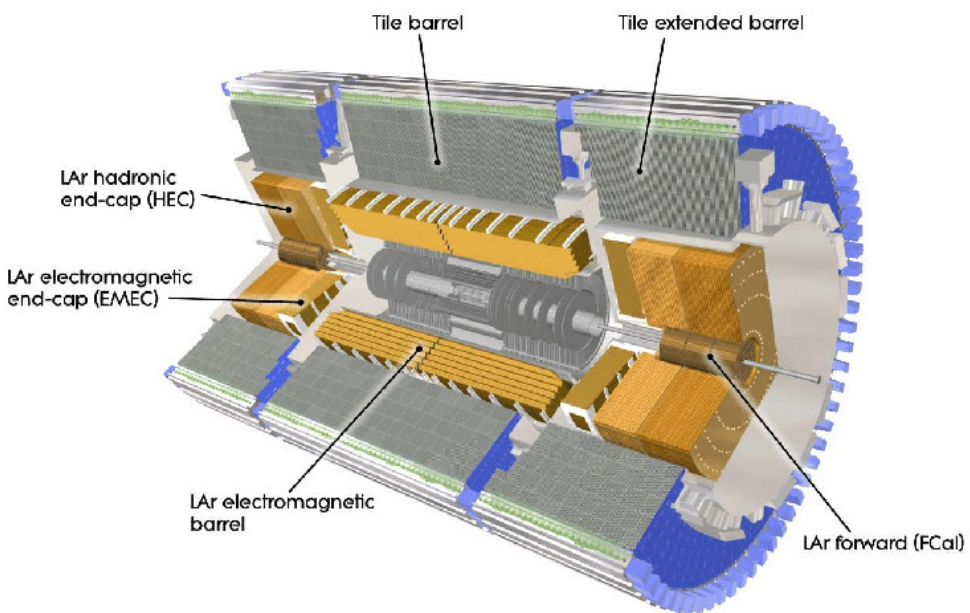


Figure 5.3: Cutaway view of the calorimeter system of the ATLAS detector [].

229 Situated outside the Inner Detector are two concentric calorimeters. The inner calorimeter
 230 uses liquid argon (LAr) to measure energy of particles that interact electromagnetically, which
 231 includes photons and any charged particle. The LAr calorimeter is made of heavy metals,
 232 primarily lead and copper, which causes electromagnetically interacting particles to shower,
 233 depositing their energy in the detector. The showering of the high energy particles that pass

234 through calorimeter cause the liquid argon to ionize, and the ionized electrons are detected by
235 electronic readouts. The LAr calorimeter consists of around 180,000 readout channels.

236 The outer calorimeter measures the energy from particles that pass through the EM calor-
237 imeter, and measures the energy of particles that interact via the strong force. This is primarily
238 hadrons. It is composed of steel plates to cause hadronic showering and scintillating tiles as the
239 active material. The signals from the hadronic calorimeter are read out by photomultiplier tubes
240 (PMTs).

241 **5.3 Muon Spectrometer**

242 Because muons are heavier than electrons and photons, and do not interact via the strong force,
243 they generally pass through the detector without being stopped by the calorimeters. The outermost
244 components of the detector are designed specifically to measure the energy and momentum of
245 muons produced in the LHC. The muon spectrometer consists of tracking and triggering system.
246 It extends from the outside of the calorimeter system, about a 4.25 m radius from the beam line,
247 to a radius of 11 m. This large detector system is necessary to accurately measure the momentum
248 of muons, which is essential not only for measurements involving the muons themselves, but also
249 to accurately estimate the missing energy in each event.

250 Two large toroidal magnets within the muon system generate a large magnetic field which
251 covers an area 26 m long with a radius of 10 m. Because the area covered by this magnet system
252 is so large, a uniform magnetic field like the one produced in the Inner Detector is impractical.

253 Instead, the magnetic field that exists in the muon spectrometer ranges between 2 T and 8 T, and
254 is much less uniform. The path of the muons passing through the spectrometer is bent by this
255 field, allowing their charge to be determined.

256 1200 tracking chambers are placed in the muon system in order to precisely measure the
257 tracks of muons with high spatial resolution.

258 **5.4 Trigger System**

259 Because of the high collision rate and large amount of data collected by the various subdetectors,
260 ATLAS produces far more data than can actually be stored. Each event produces around 25 Mb
261 of raw data, which multiplied by the bunch crossing rate of 40 MHz, comes out to around a
262 petabyte of data every second. The information from every event cannot practically be stored,
263 therefore a sophisticated trigger system is employed in real time to determine whether events are
264 sufficiently interesting to be worth storing.

265 The trigger system in ATLAS involves multiple levels, each of which select out which
266 events move on to the next level of scrutiny. The level-1 trigger uses hardware information from
267 the calorimeters and muon spectrometer to select events that contain candidates for particles
268 commonly used in analysis, such as energetic leptons and jets. The level-1 trigger reduces the
269 rate of events from 40 MHz to around 100 kHz.

Events that pass the level-1 trigger move to the High-Level Trigger (HLT). The HLT takes place outside of the detector in software, and looks for properties such as a large amount of missing transverse energy, well defined leptons, and multiple high energy jets. Events that pass the HLT are stored and used for analysis. Because the specifics of the HLT are determined by software rather than hardware, the thresholds can be changed throughout the run of the detector in response to run conditions such as changes to pileup and luminosity. After the HLT is applied, the event rate is reduced to around 1000 per second, which are recorded for analysis.

Part IV

Search for Dimension-Six Operators

6 Data and Monte Carlo Samples

For both data and Monte Carlo (MC) simulations, samples were prepared in the xAOD format, which was used to produce a xAOD based on the HIGG8D1 derivation framework. This framework was designed for the main $t\bar{t}H$ multi-lepton analysis. Because this analysis targets events with multiple light leptons, as well as tau hadrons, this framework skims the dataset of any events that do not meet at least one of the following requirements:

- at least two light leptons within a range $|\eta| < 2.6$, with leading lepton $p_T > 15$ GeV and subleading lepton $p_T > 5$ GeV

- 287 • at least one light lepton with $p_T > 15$ GeV within a range $|\eta| < 2.6$, and at least two hadronic
288 taus with $p_T > 15$ GeV.

289 Samples were then generated from these HIGG8D1 derivations using a modified version of
290 AnalysisBase version 21.2.127.

291 **6.1 Data Samples**

292 The study uses proton-proton collision data collected by the ATLAS detector from 2015 through
293 2018, which represents an integrated luminosity of 139 fb^{-1} and an energy of $\sqrt{s} = 13 \text{ TeV}$. All
294 data used in this analysis was included in one the following Good Run Lists:

- 295 • data15_13TeV.periodAllYear_DetStatus-v79-repro20-02_DQDefects-00-02-02
296 _PHYS_StandardGRL_All_Good_25ns.xml
- 297 • data16_13TeV.periodAllYear_DetStatus-v88-pro20-21_DQDefects-00-02-04
298 _PHYS_StandardGRL_All_Good_25ns.xml
- 299 • data17_13TeV.periodAllYear_DetStatus-v97-pro21-13_Unknown_PHYS_StandardGRL
300 _All_Good_25ns_Triggerno17e33prim.xml
- 301 • data18_13TeV.periodAllYear_DetStatus-v102-pro22-04_Unknown_PHYS_StandardGRL
302 _All_Good_25ns_Triggerno17e33prim.xml

303 **6.2 Monte Carlo Samples**

304 Several Monte Carlo (MC) generators were used to simulate both signal and background pro-
 305 cesses. For all of these, the effects of the ATLAS detector are simulated in Geant4. The specific
 306 event generator used for each of these MC samples is listed in table ??.

Table 1: The configurations used for event generation of signal and background processes, including the event generator, matrix element (ME) order, parton shower algorithm, and parton distribution function (PDF).

Process	Event generator	ME order	Parton Shower	PDF
ttH	MG5_AMC (MG5_AMC)	NLO (NLO)	PYTHIA 8 (HERWIG++)	NNPDF 3.0 NLO [Ball:2014uwa] (CT10 [ct10])
t̄W	MG5_AMC (SHERPA 2.1.1)	NLO (LO multileg)	PYTHIA 8 (SHERPA)	NNPDF 3.0 NLO (NNPDF 3.0 NLO)
t̄t(Z/γ* → ll)	MG5_AMC	NLO	PYTHIA 8	NNPDF 3.0 NLO
VV	SHERPA 2.2.2	MEPS NLO	SHERPA	CT10
t̄t	POWHEG-BOX v2 [powhegtt]	NLO	PYTHIA 8	NNPDF 3.0 NLO
t̄tγ	MG5_AMC	LO	PYTHIA 8	NNPDF 2.3 LO
tZ	MG5_AMC	LO	PYTHIA 6	CTEQ6L1
tHqb	MG5_AMC	LO	PYTHIA 8	CT10
tHW	MG5_AMC (SHERPA 2.1.1)	NLO (LO multileg)	HERWIG++ (SHERPA)	CT10 (NNPDF 3.0 NLO)
tWZ	MG5_AMC	NLO	PYTHIA 8	NNPDF 2.3 LO
t̄t̄t, t̄t̄t̄t	MG5_AMC	LO	PYTHIA 8	NNPDF 2.3 LO
t̄tW+W-	MG5_AMC	LO	PYTHIA 8	NNPDF 2.3 LO
s-, t-channel, Wt single top	POWHEG-BOX v1 [powhegstp]	NLO	PYTHIA 6	CT10
qqVV, VVV				
Z → l+l-	SHERPA 2.2.1	MEPS NLO	SHERPA	NNPDF 3.0 NLO

307 **7 Object Reconstruction**

308 All analysis channels considered in this note share a common object selection for leptons and
 309 jets, as well as a shared trigger selection.

³¹⁰ **7.1 Trigger Requirements**

³¹¹ Events are required to be selected by dilepton triggers, as summarized in table ??.

Dilepton triggers (2015)	
$\mu\mu$ (asymm.)	HLT_mu18_mu8noL1
ee (symm.)	HLT_2e12_lhloose_L12EM10VH
$e\mu, \mu e$ (\sim symm.)	HLT_e17_lhloose_mu14
Dilepton triggers (2016)	
$\mu\mu$ (asymm.)	HLT_mu22_mu8noL1
ee (symm.)	HLT_2e17_lhvloose_nod0
$e\mu, \mu e$ (\sim symm.)	HLT_e17_lhloose_nod0_mu14
Dilepton triggers (2017)	
$\mu\mu$ (asymm.)	HLT_mu22_mu8noL1
ee (symm.)	HLT_2e24_lhvloose_nod0
$e\mu, \mu e$ (\sim symm.)	HLT_e17_lhloose_nod0_mu14
Dilepton triggers (2018)	
$\mu\mu$ (asymm.)	HLT_mu22_mu8noL1
ee (symm.)	HLT_2e24_lhvloose_nod0
$e\mu, \mu e$ (\sim symm.)	HLT_e17_lhloose_nod0_mu14

Table 2: List of lowest p_T -threshold, un-prescaled dilepton triggers used for 2015-2018 data taking.

³¹² **7.2 Light Leptons**

³¹³ Electron candidates are reconstructed from energy clusters in the electromagnetic calorimeter that
³¹⁴ are associated with charged particle tracks reconstructed in the inner detector [**ATLAS-CONF-2016-024**].
³¹⁵ Electron candidates are required to have $p_T > 10$ GeV and $|\eta_{\text{cluster}}| < 2.47$. Candidates in the
³¹⁶ transition region between different electromagnetic calorimeter components, $1.37 < |\eta_{\text{cluster}}| <$
³¹⁷ 1.52, are rejected. A multivariate likelihood discriminant combining shower shape and track

318 information is used to distinguish prompt electrons from nonprompt leptons, such as those
319 originating from hadronic showers.

320 To further reduce the non-prompt contribution, the track of each electron is required to
321 originate from the primary vertex; requirements are imposed on the transverse impact parameter
322 significance ($|d_0|/\sigma_{d_0}$) and the longitudinal impact parameter ($|\Delta z_0 \sin \theta_\ell|$), as shown in table
323 ??.

324 Muon candidates are reconstructed by combining inner detector tracks with track segments
325 or full tracks in the muon spectrometer [**PERF-2014-05**]. Muon candidates are required to have
326 $p_T > 10$ GeV and $|\eta| < 2.5$. All leptons are required to be isolated, and pass a non-prompt BDT
327 selection described in detail in [**ttH_paper**].

328 7.3 Jets

329 Jets are reconstructed from calibrated topological clusters built from energy deposits in the
330 calorimeters [**ATL-PHYS-PUB-2015-015**], using the anti- k_t algorithm with a radius parameter
331 $R = 0.4$. Jets with energy contributions likely arising from noise or detector effects are removed
332 from consideration [**ATLAS-CONF-2015-029**], and only jets satisfying $p_T > 25$ GeV and
333 $|\eta| < 2.5$ are used in this analysis. For jets with $p_T < 60$ GeV and $|\eta| < 2.4$, a jet-track
334 association algorithm is used to confirm that the jet originates from the selected primary vertex,
335 in order to reject jets arising from pileup collisions [**PERF-2014-03**].

³³⁶ 7.4 Missing Transverse Energy

³³⁷ Because all $t\bar{t}H - ML$ channels considered include multiple neutrinos, missing transverse
³³⁸ energy (E_T^{miss}) is present in each event. The missing transverse momentum vector is defined as
³³⁹ the inverse of the sum of the transverse momenta of all reconstructed physics objects as well
³⁴⁰ as remaining unclustered energy, the latter of which is estimated from low- p_T tracks associated
³⁴¹ with the primary vertex but not assigned to a hard object [ATL-PHYS-PUB-2015-027].

³⁴² 8 Higgs Momentum Reconstruction

³⁴³ Reconstructing the momentum of the Higgs boson is a particular challenge for channels with
³⁴⁴ leptons in the final state: Because all channels include at least two neutrinos in the final state, the
³⁴⁵ Higgs can never be fully reconstructed. However, the momentum spectrum can be well predicted
³⁴⁶ by a neural network when provided with the four-vectors of the Higgs Boson decay products,
³⁴⁷ as shown in section ???. With this in mind, a sophisticated approach involving several layers of
³⁴⁸ MVAs is used to reconstruction the Higgs momentum.

³⁴⁹ The first layer is a Neural Network designed to select which jets are most likely to be
³⁵⁰ the b-jets that came from the top decay. The kinematics of these jets are fed into the second
³⁵¹ layer, also a BDT, which is designed to identify the decay products of the Higgs Boson itself.
³⁵² The kinematics of these particles are then fed into a deep neural-network, which predicts the
³⁵³ momentum of the Higgs.

354 **8.1 Truth Level Reconstruction**

355 Machine Learning algorithms are trained to identify the decay products of the Higgs Boson
356 using MC simulations of $t\bar{t}H$ events. Reconstructed physics objects are matched to truth level
357 particles, in order to identify the parents of these reconstructed objects.

358 **8.2 b-jet Identification**

359 Including the kinematics of the b-jets that originate from the top decay is found to improve the
360 identification of the Higgs decay products, and improve the accuracy with which the Higgs
361 momentum can be reconstructed. Because these b-jets are reconstructed by the detector with
362 high efficiency (just over 90% of the time), and can be identified relatively consistently, the first
363 step in reconstructing the Higgs is selecting the b-jets from the top decay.

364 Exactly two b-jets are expected in the final state of $t\bar{t}H - ML$ events. However, in both
365 the 3l and 2lSS channels, only one or more b-tagged jets are required (where the 70% DL1r b-tag
366 working point is used). Therefore, for events which have exactly one, or more than two, b-tagged
367 jets, deciding which combination of jets correspond to the top decay is non-trivial. Further,
368 events with 1 b-tagged jet represent just over half of all $t\bar{t}H - ML$ events. Of those, both b-jets
369 are reconstructed by the detector 70% of the time. Therefore, rather than adjusting the selection
370 to require exactly 2 b-tagged jets, and losing more than half of the signal events, a neural network
371 is used to predict which pair of jets is most likely to correspond to truth b-jets.

372 The kinematics of each possible pairing of jets are used to train the network, where the
373 pairing that includes both truth b-jets is assigned a label of 1, and all other pairings a label of 0.
374 Further details concerning the models, including the specific input variables, hyperparameters,
375 and performance metrics, can be found in ??

376 For each event, all pairings of jets are fed into the model, and the pair of jets with the
377 highest output score are taken to be b-jets in successive steps of the analysis. This procedure is
378 found to identify the correct pairing of jets for 73% of 2lSS signal events, and 78% of 3l signal
379 events.

380 **8.3 Higgs Reconstruction**

381 Techniques similar to the b-jet identification algorithms are employed to select the decay products
382 of the Higgs.

383 **8.4 p_T Prediction**

384 Once the most probable decay products have been identified, their kinematics are used to recon-
385 struct the momentum spectrum of the Higgs Boson.

386 8.5 3l Decay Mode

387 In the 3l channel, there are two possible ways for the Higgs to decay, both involving intermediate
388 W boson pairs: Either both W bosons decay leptonically, in which case the reconstructed decay
389 consists of two leptons (referred as the fully-leptonic 3l channel), or one W decays leptonically
390 and the other hadronically, giving two jets and one lepton in the final state (referred to as the
391 semi-leptonic 3l channel). In order to accurately reconstruct the Higgs, it is necessary to identify
392 which of these decays took place for each 3l event.

393 9 Signal Region Definitions

394 Events are divided into two channels based on the number of leptons in the final state: one with
395 two same-sign leptons, the other with three leptons. The 3l channel includes events where both
396 leptons originated from the Higgs boson as well as events where only one of the leptons

397 9.1 Pre-MVA Event Selection

398 A preselection is applied to define orthogonal analysis channels based on the number of leptons
399 in each event.

400 **9.1.1 2lSS Channel**

401 **9.1.2 3l Channel**

402 **9.2 Event MVA**

403 Separate multi-variate analysis techniques (MVAs) are used in order to distinguish signal events
404 from background for each analysis channel - 2lSS, 3l semi-leptonic, and 3l fully leptonic. In
405 particular, Neural Networks produced with Tensorflow are trained using the kinematics of signal
406 and background events derived from Monte Carlo simulations. Further, because the background
407 composition differs for events with a high reconstructed Higgs p_T compared to events with low
408 reconstructed Higgs p_T , separate MVAs are produced for high and low p_T regions.

409 Output distributions of each MVA are shown in figure ???. Detailed explanations of each
410 of the models can be found in section ???.

411 **9.3 Signal Region Definitions**

412 Once pre-selection has been applied, channels are further refined based on the MVAs described
413 above. The output of the model described in section ??? is used to separate the three channel
414 into two - Semi-leptonic and Fully-leptonic - based on the predicted decay mode of the Higgs
415 boson.

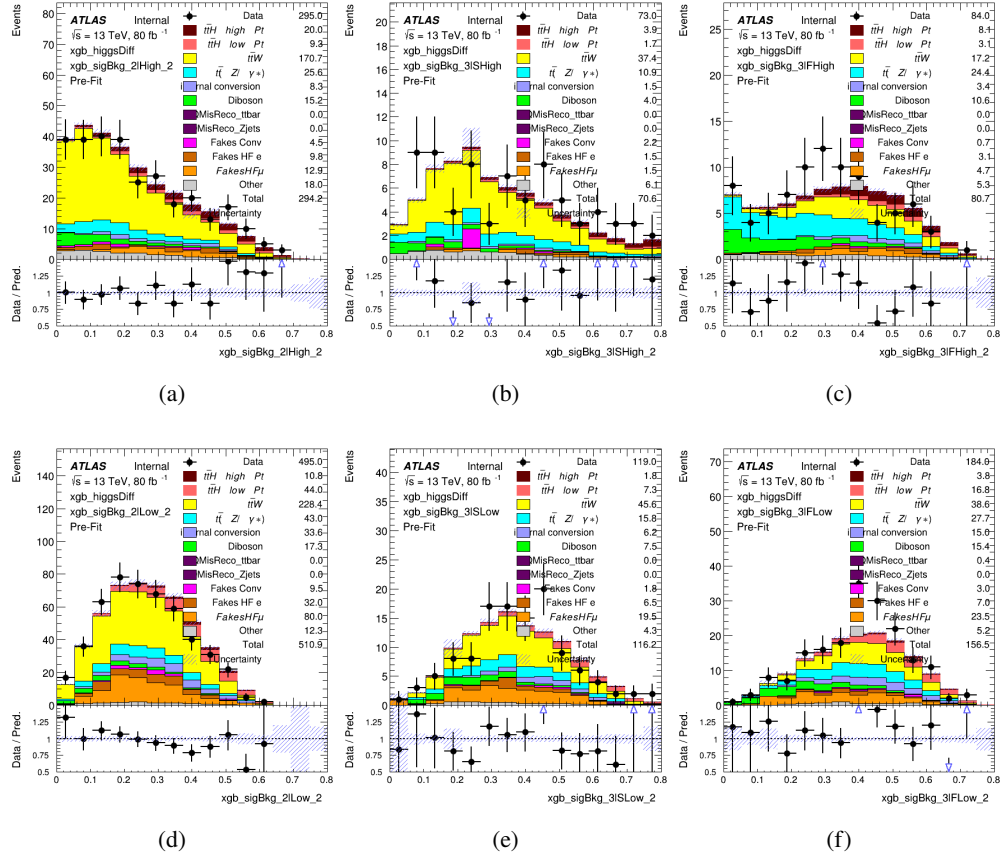


Figure 9.1: scores

416 For each event, depending on the channel as well as the predicted p_T of the Higgs derived
 417 from the algorithm described in section ??, a cut on the appropriate background rejection
 418 algorithm is applied. The specific selection used, and the event yield in each channel after this
 419 selection has been applied, is summarized below.

420 **9.3.1 2lSS**

421 **9.3.2 3l – Semi – leptonic**

422 **9.3.3 3l – Fully – leptonic**

423 **10 Background Rejection MVA**

424 **10.1 Background Rejection MVAs**

425 Separate mdoels are used in order to distinguish signal events from background for each analysis
426 channel - 2lSS, 3l semi-leptonic, and 3l fully leptonic. In particular, Neural Networks produced
427 with Tensorflow are trained using the kinematics of signal and background events derived from
428 Monte Carlo simulations. Further, because the background composition differs for events with
429 a high reconstructed Higgs p_T compared to events with low reconstructed Higgs p_T , separate
430 MVAs are produced for high and low p_T regions.

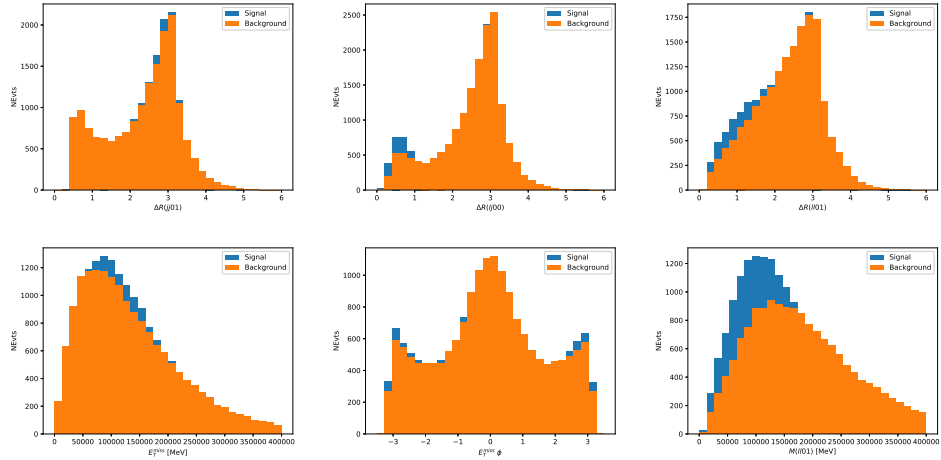


Figure 10.1:

431 **10.1.1 2lSS - High p_T**

432 **10.1.2 2lSS - Low p_T**

433 **10.1.3 3l Semi-Leptonic - High p_T**

434 **10.1.4 3l Semi-Leptonic - Low p_T**

435 **10.1.5 3l Fully Leptonic - High p_T**

436 **10.1.6 3l Fully Leptonic - Low p_T**

437 **11 Systematic Uncertainties**

438 The systematic uncertainties that are considered are summarized in table ???. These are imple-
439 mented in the fit either as a normalization factors or as a shape variation or both in the signal
440 and background estimations. The numerical impact of each of these uncertainties is outlined in
441 section ??.

442 The uncertainty in the combined 2015+2016 integrated luminosity is derived from a
443 calibration of the luminosity scale using x-y beam-separation scans performed in August 2015
444 and May 2016 [[lumi](#)].

Table 3: Sources of systematic uncertainty considered in the analysis. Some of the systematic uncertainties are split into several components, as indicated by the number in the rightmost column.

Systematic uncertainty	Components
Luminosity	1
Pileup reweighting	1
Physics Objects	
Electron	6
Muon	15
Jet energy scale and resolution	28
Jet vertex fraction	1
Jet flavor tagging	131
E_T^{miss}	3
Total (Experimental)	186
Background Modeling	
Cross section	24
Renormalization and factorization scales	10
Parton shower and hadronization model	2
Shower tune	4
Total (Signal and background modeling)	40
Background Modeling	
Cross section	24
Renormalization and factorization scales	10
Parton shower and hadronization model	2
Shower tune	4
Total (Signal and background modeling)	40
Total (Overall)	226

445 The experimental uncertainties are related to the reconstruction and identification of light
 446 leptons and b-tagging of jets, and to the reconstruction of E_T^{miss} . The sources which contribute
 447 to the uncertainty in the jet energy scale [**jes**] are decomposed into uncorrelated components and
 448 treated as independent sources in the analysis.

449 The uncertainties in the b-tagging efficiencies measured in dedicated calibration analyses
 450 [**btag_cal**] are also decomposed into uncorrelated components. The large number of components
 451 for b-tagging is due to the calibration of the distribution of the BDT discriminant.

452 The systematic uncertainties associated with the signal and background processes are

453 accounted for by varying the cross-section of each process within its uncertainty.

454 **12 Results**

455 A maximum likelihood fit is performed simultaneously over the regions described in section

456 **??.**

457 **Part V**

458 **Conclusion**

459 As search for the effects of dimension-six operators on $t\bar{t}H$ production is performed. An effective

460 field theory approached is used to parameterize the effects of high energy physics on the Higgs

461 momentum spectrum. The momentum spectrum is reconstructed using various MVA techniques,

462 and the limits on dimension-six operators are limited to X.

463 List of contributions

464

465 Appendices

466 A Machine Learning Models

467 The following section provides details regarding the various machine learning models used in
468 the analysis. The Keras neural network framework, with Tensorflow as the backend, is used
469 to create each model, and the number of hidden layers and nodes are determined using grid
470 search optimization. For each model, a LeakyReLU activation function is used, along with a
471 learning rate of 0.01, and the Adam optimization algorithm. For the classification algorithms
472 (b-jet matching, Higgs reconstruction, and background separation) binary-cross entropy is used
473 as the loss function.

474 A.1 b-jet Identification Algorithms

475 A.1.1 2lSS Channel

476 For the 2lSS channel, the following input features as used for training:

477 Based on the results of grid search evaluation, the optimal architecture is found to include
478 5 hidden layers with 40 nodes each. A learning rate of 0.01 is used, and leakyReLU is used as
479 an activation function. The output score distribution as well as the ROC curve for the trained
480 model are shown in figure ??.

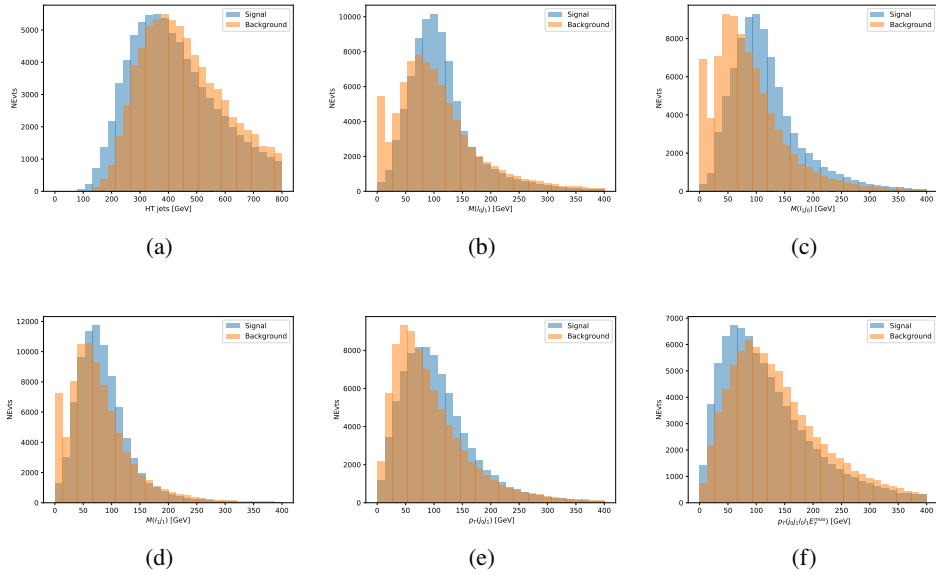


Figure A.1: Input features for top2lSS training

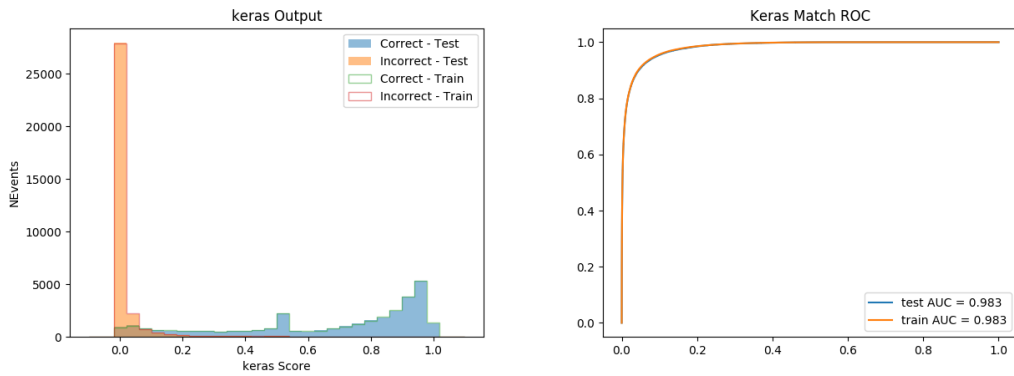


Figure A.2: (left) the output score of the NN for correct and incorrect combinations of jets. (right) the ROC curve...

$M(j_0 j_1)$	$M(j_0 j_1 l_0 l_1 E_T^{\text{miss}})$	$M(l_0 j_0)$
$M(l_0 j_1)$	$M(l_1 j_0)$	$M(l_1 j_1)$
$p_T(j_0 j_1 l_0 l_1 E_T^{\text{miss}})$	$\Delta\phi(j_0)(E_T^{\text{miss}})$	$\Delta\phi(j_1)(E_T^{\text{miss}})$
$\Delta R(j_0)(j_1)$	$\Delta R(j_0 l_0)(j_1 l_1)$	$\Delta R(j_0 l_1)(j_1 l_0)$
$\Delta R(l_0)(j_0)$	$\Delta R(l_0)(j_1)$	$\Delta R(l_1)(j_0)$
$\Delta R(l_1)(j_1)$	jet DL1r 0	jet DL1r 1
jet η 0	jet η 1	jet p_T 0
jet p_T 1	jet rankDL1r 0	jet rankDL1r 1
Lepton p_T 0	Lepton p_T 1	E_T^{miss}
nJets	nJets OR DL1r 60	nJets OR DL1r 85

Table 4: Input features used in the 2ISS b-jet identification algorithm

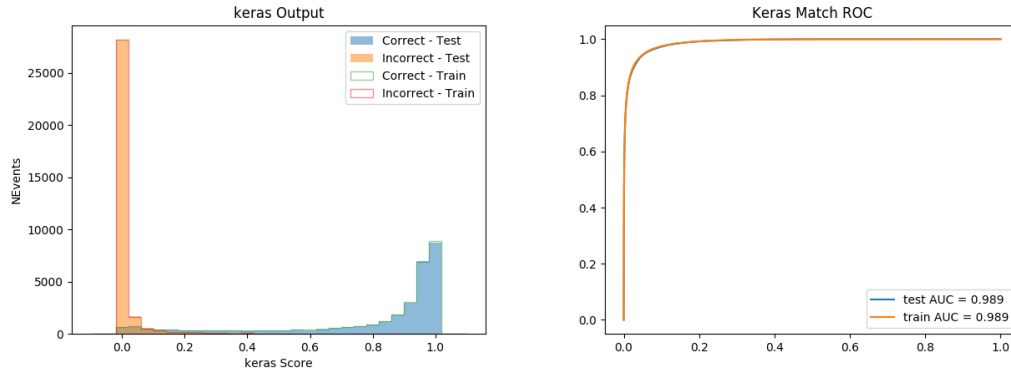


Figure A.3: tmp

481 **A.1.2 3l Channel**

482 Based on the results of grid search evaluation, the optimal architecture is found to include 5
 483 hidden layers with 40 nodes each. The output score distribution as well as the ROC curve for the
 484 trained model are shown in figure ??.

485 **A.2 Higgs Reconstruction Algorithms**

486 **A.2.1 2lSS Channel**

487 **A.2.2 3l Semi-leptonic Channel**

488 **A.2.3 3l Fully-leptonic Channel**

489 **A.3 p_T Prediction MVA**

490 **A.3.1 2lSS Channel**

491 **A.3.2 3l Semi-leptonic Channel**

492 **A.3.3 3l Fully-leptonic Channel**

493 **A.4 3l Decay MVA**

494 **A.5 Background Rejection MVAs**

495 Separate mdoels are used in order to distinguish signal events from background for each analysis
496 channel - 2lSS, 3l semi-leptonic, and 3l fully leptonic. In particular, Neural Networks produced
497 with Tensorflow are trained using the kinematics of signal and background events derived from
498 Monte Carlo simulations. Further, because the background composition differs for events with

- 499 a high reconstructed Higgs p_T compared to events with low reconstructed Higgs p_T , separate
 500 MVAs are produced for high and low p_T regions.

501 **A.5.1 2lSS - High p_T**

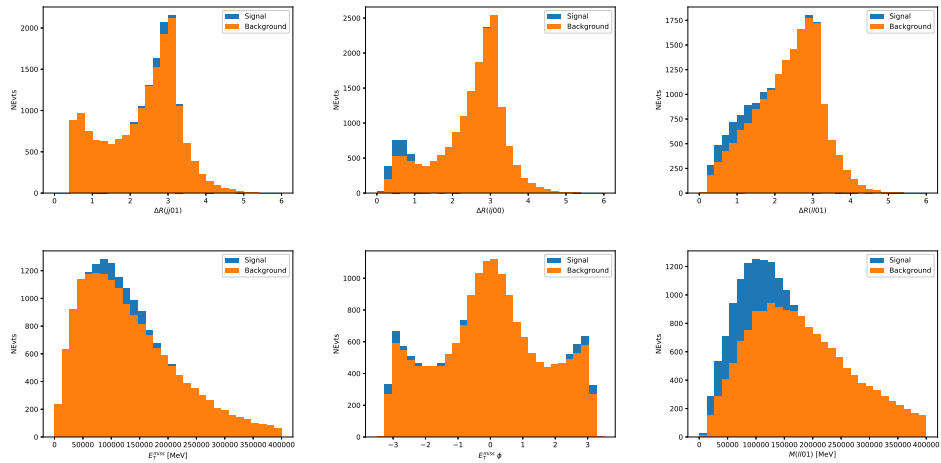


Figure A.4:

502 **A.5.2 2lSS - Low p_T**

503 **A.5.3 3l Semi-Leptonic - High p_T**

504 **A.5.4 3l Semi-Leptonic - Low p_T**

505 **A.5.5 3l Fully Leptonic - High p_T**

506 **A.5.6 3l Fully Leptonic - Low p_T**

507 **B**